



HAL
open science

Determination of the longitudinal thermal conductivity of low-ordered carbon fibers by using an optothermal Raman technique

Atin Kumar, M.R. Ammar, A. Canizarès, Jérôme Vicente, Benoit Rousseau

► **To cite this version:**

Atin Kumar, M.R. Ammar, A. Canizarès, Jérôme Vicente, Benoit Rousseau. Determination of the longitudinal thermal conductivity of low-ordered carbon fibers by using an optothermal Raman technique. *Journal of Raman Spectroscopy*, 2024, 55 (1), pp.86-98. 10.1002/jrs.6616 . hal-04309217

HAL Id: hal-04309217

<https://hal.science/hal-04309217v1>

Submitted on 28 Nov 2024

HAL is a multi-disciplinary open access archive for the deposit and dissemination of scientific research documents, whether they are published or not. The documents may come from teaching and research institutions in France or abroad, or from public or private research centers.

L'archive ouverte pluridisciplinaire **HAL**, est destinée au dépôt et à la diffusion de documents scientifiques de niveau recherche, publiés ou non, émanant des établissements d'enseignement et de recherche français ou étrangers, des laboratoires publics ou privés.

Determination of the Longitudinal Thermal Conductivity of Low Ordered Carbon Fibers by using an Optothermal Raman Technique

A. Kumar^{1,2} | M.R. Ammar³ | A. Canizarés⁴ | J. Vicente⁵ | B. Rousseau¹

Abstract

The usage of carbon fibers (CF) for high temperature applications has been increasing in recent years. However, the determination of thermal properties at high temperatures is a challenging task. In this study, the thermal conductivity of two different types of CF having a diameter in the range from 5-7 μm , as a function of temperature, was examined by using the Optothermal Raman method. Raman spectroscopy was first used to obtain the structural organization and structural homogeneity of the fibers. Then, owing to the fact that Raman spectra are sensitive to laser excitation power and external temperature, Raman spectroscopy was used as a contactless thermometer to determine the local temperature rise of the fibers. A formula was derived by solving the heat diffusion equation for cylindrical fibers, and a set of boundary conditions, similar to the experimental conditions, which allows accurate estimation of longitudinal thermal conductivity. The results are discussed in relation with the phonon scattering theory and can be attributed to the combined effect of scattering from defects. The radiative and convective heat losses were estimated, and their influence on thermal conductivity was also determined.

KEYWORDS

Carbon fibers, Thermal conductivity, Raman mapping, Optothermal Raman, High Temperature Measurements

1 | INTRODUCTION

Carbon fibers (CF) play a vital role in the design of various engineering systems because of their remarkable mechanical, chemical, and thermal properties. Advanced materials made of CF such as carbon-carbon composites, carbon fiber reinforced composites, and reinforced carbon-carbon are widely used as filtration membranes [1], electrodes of fuel cells [2, 3], braking systems in aerospace and automotive industries [4, 5], and thermal protection systems [6–10]. With continuous advancement in material technology, study of thermal properties of these materials has been an interesting topic for researchers and industrialists.

Many efforts have been devoted to correctly estimate the thermal properties (e.g., specific heat capacity, thermal diffusivity, thermal conductivity, etc.) of above mentioned materials at different scales either through experimental [9, 11], or numerical means [7–9, 12, 13]. Although, the methods to estimate thermal properties at macroscopic scale have been discussed in numerous studies, very limited information for microscopic materials such as CF can be found. This is not only due to the microscopic size of the fibers which requires advanced tools, but also due to the large variation of the thermal conductivity of these materials with temperature and their structural organization.

Generally, there are two categories of methods to determine the thermal conductivity of fibers: steady state methods and transient methods. These methods may use different heat sources (electrical or optical), and different temperature detection techniques (with or without contact) to determine the thermal conductivity. For instance, Laser flash method [14] uses a bundle of fibers to approximate the thermal conductivity of a single fiber. However, methods such as AC calorimetry [15, 16], direct method [17], photorefectance [18], 3ω method [19–23], T-type probe method [24], modified laser flash method [25], Angstrom method [26], etc. are used to determine the thermal conductivity of a single fiber. A detailed description of these methods along with several other methods used for measurement of thermal conductivity can be found in these references [27, 28]. Each method comes with one or more advantages over the other in terms of heating method, experiment time, ease of use, data processing methods, handling, and preparation of samples. According to the choice of the method, certain limitations can be faced during the measurement, and can not be used if the fibers are too fragile, short in length, structurally heterogeneous, have low electric conductivity, and rough surface. Thereby, raising questions over the feasibility and accuracy of the method. In general, a method can be considered robust and feasible if it can deal with all these challenges, and yet provides the result with high accuracy.

In view of the above discussion, an optical method based on Raman spectroscopy is proposed for the determination of the thermal conductivity of CF. The method is contactless and non destructive which can be applied over a very small fiber (having a diameter in the range from 5-7 μm and length of the order of 1 mm) with minimal sample preparation. This is a steady state method, introduced by Périchon et al. in 1999 to measure the thermal conductivity of poor heat-conducting materials and thin films (e.g., porous silicon) [29, 30]. Balandin et al. in 2008 [31] further developed the methodology and expressions to determine the thermal conductivity of single layer graphene (SLG) which is highly conductive, since then it is being used by many researchers [32–41]. This method is also known as Optothermal Raman (OTR) method. In this method, the Raman laser is used as a local heat source resulting in temperature rise at a spot, and the resulting Raman spectra, which are sensitive to the variation of temperature [42], are processed in a way to use Raman spectroscopy as a “thermometer”. For the determination of thermal conductivity, a thermal model has been developed by solving the heat diffusion equation for a case of cylindrical geometry with very high aspect ratio (i.e., length \gg diameter) and satisfying the suitable boundary conditions. Here, this method is used to measure the thermal conductivity of two different CF characterized by low structural order. The capabilities of OTR method has been further extended to determine the thermal conductivity at high temperatures up to 1300 K.

2 | MATERIALS AND EXPERIMENTAL SETUP

Two different CF extracted from different sources, were used in this study. First one was PAN-based carbon fiber (p-CF) (T300 from Toray Industries [43]), and second one was Rayon-based carbon fiber (r-CF). The fibers had a diameter in the range from 5-7 μm , and were approximately 1 mm in length. rayon-based carbon fiber (r-CF) were initially heat treated at 2500 K, however, the initial heat treatment temperature of PAN-based carbon fiber (p-CF) was not provided by the manufacturer. Both types of fibers were first analyzed to confirm the structural homogeneity at micrometer scale using Raman mapping, and then the OTR technique was used to determine the thermal conductivity of the fibers in the steady state regime.

2.1 | Raman scattering measurements

Raman spectroscopy measurement was performed using Renishaw inVia Qontor spectrometer equipped with Ar⁺ laser (2.41 eV/ 514.5 nm). The excitation laser was a diode pumped solid state laser (Cobalt Blues) with a maximum output of 60 mW. A grating of 1800 lines/mm was used to disperse the scattered light before being detected by the charged coupled device (CCD) camera. The spectra were obtained under an optical microscope Leica DM 2500 with $\times 50$ long working distance objective

which has a numerical aperture of 0.50. For analysis, a very small laser excitation power (≈ 0.5 mW) was used to avoid any laser induced heating. Quantitative information was retrieved from the deconvolution of the peaks using conventional curve fitting procedure. The best fit was found with a combination of Voigt and Breit-Wigner-Fano (BWF) curves by using Focus software [44]. Quantities such as peak position (ω), peak intensity (I), and full width at half maximum (FWHM) were obtained to analyze the data. Furthermore, to obtain a complete picture of structural distribution, Raman mapping was used. The Raman spectrum obtained at a point was used as a reference and then direct classical least square (DCLS) method was used to reconstruct the complete image of structural distribution by taking a linear combination of collected spectra from a reference spectrum.

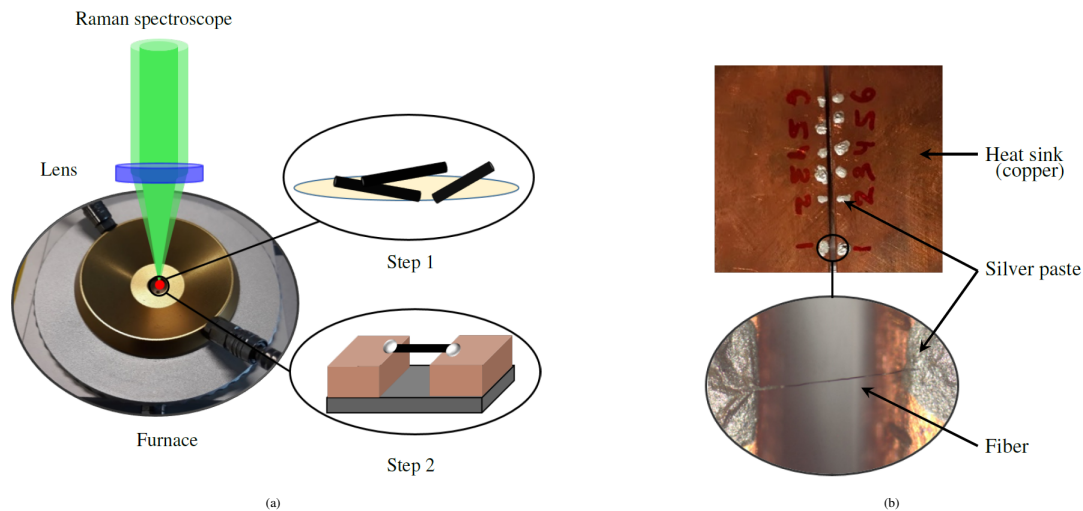


FIGURE 1 Schematic of OTR technique; (a) The fibers were placed inside the furnace which allows uniform heating in controlled atmosphere. In step 1, the fibers were dispersed over a borosilicate glass plate, and in step 2, the junction over which the fibers were suspended, was placed inside the furnace to heat the fibers in a controlled environment; (b) An optical microscopy image of sample holder (at the top), and a zoomed view of the suspended fiber (at the bottom).

2.2 | Determination of temperature difference using Optothermal Raman technique

The measurement of thermal conductivity using OTR technique requires additional equipment along with the Raman spectroscopy setup. For external heating of fibers, a Linkam TS 1500 system capable of heating up to 1773 K with a precision of ± 1 K was used. The temperature was regulated externally, and the Raman spectra were recorded at an interval of 25 K. The fibers were dispersed over a borosilicate glass plate as shown in figure 1a, step 1, and were heated at the rate of 15 K/min. The fibers were kept at a particular temperature for ≈ 4 min to achieve thermal equilibrium, before recording the spectra. Some additional precautions were taken such as the focus of the laser was checked before and after the acquisition in order to avoid any unexpected defocusing and drifting of laser spot because of thermal expansion caused by heating. Also, to avoid oxidation at high temperatures, the fibers were heated under argon (inert) gas environment.

Furthermore, a sample holder was designed, as shown in figure 1a, step 2. Two copper slabs were stuck over a glass base maintained at a distance of 0.5 mm from each other, and the fibers were suspended between them. A silver paste was used to establish proper contact between the fibers and copper slabs to neglect contact resistance. Although the fibers were heated using laser power, the sample holder was kept inside the furnace to maintain a controlled environment. For statistical representation, 4-5 fibers were examined and average thermal conductivity value was retrieved. For better understanding, an optical image of the

suspended fibers is shown in figure 1b. For the particular case of r-CF, which were heated up to 1300 K, a 488 nm laser was used to reduce the contribution of thermal emission at high temperatures.

3 | METHODOLOGY, RESULTS, AND DISCUSSION

3.1 | Structural characterization using Raman mapping

Figure 2 shows the optical image of one of two CF used in this study, namely r-CF, deposited on a silicon substrate. It also shows the corresponding first order Raman spectrum and its best fit. This optical image gives an approximate information about the size and cylindrical shape of the CF. The first-order Raman spectrum of the CF (or any sp^2 carbon, in general), at any point, consists of several bands namely D, G, and D'. The G-band is due to the collective in-plane bond stretching of all pairs of sp^2 carbon atoms with E_{2g} symmetry at 1st Brillouin zone center [45–47]. Generally, the peak position of G-band of graphite is found at 1581 cm^{-1} , but due to phonon confinement effect, a shift towards a higher wavenumber (up to 1600 cm^{-1}) can be noticed [48]. The D-band corresponds to the breathing mode of aromatic carbons (A_{1g} symmetry). The band is originated from the peculiar electron-phonon-defect interaction, and is also known as the defect-band. The peak position of this band is found at around 1350 cm^{-1} when an excitation laser of wavelength equal to 514.5 nm is used. It is to be noted that the position of D-band is very sensitive to excitation energy ($\approx 50\text{ cm}^{-1}\text{ eV}^{-1}$), but the symmetry-allowed G-peak position remains unaffected by it. Furthermore, the D'-band corresponding to the phonons near the 1st Brillouin zone center also gets activated by defects. Generally, the D- and G-bands provide significant information about the structural organization of carbon materials. For r-CF, the D- and G-bands are positioned at 1350 cm^{-1} and 1583 cm^{-1} , respectively. Also, the intensity ratio (I_D/I_G) ≈ 0.88 which is usually high for this kind of non-graphitizing carbon even after the heat treatment at a temperature as high as 2500 K. However, the width of the bands which is the characteristic of the local structural order is relatively small. High intensity ratio and low band width indicate that the r-CF are locally well structured.

As the thermal conductivity of carbon species is influenced by the structural organization of carbon matter at nanometric scale, any heterogeneity in the structure may lead to under- or over-estimation of thermal conductivity. Since the spectrum in figure 2 was obtained from a laser spot, having a diameter of $\approx 1\text{ }\mu\text{m}$, it appears valuable to assess the structural homogeneity of the fiber.

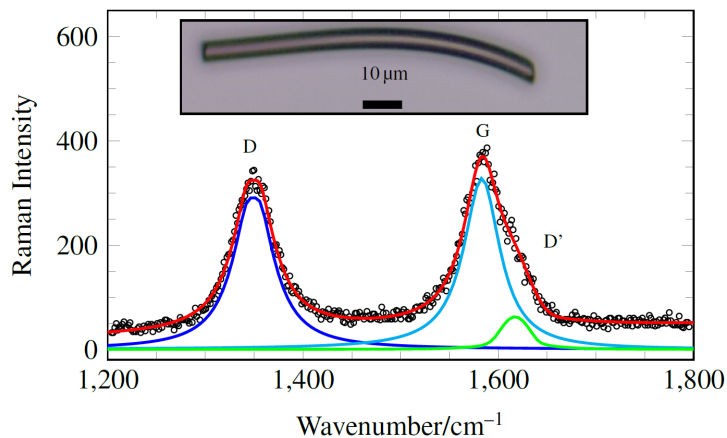


FIGURE 2 Raman spectrum of rayon-based carbon fiber (r-CF) showing D, G, and D' bands with the best fit obtained by using a combination of Voigt and Breit-Wigner-Fano (BWF) profiles (in red). A laser of 514.5 nm wavelength was used, and the spectrum was recorded at room temperature. Note: to avoid overlap, the individual bands are downshifted intentionally. The insert represents optical image of the analyzed fiber obtained from Leica DM 2500 microscope.

The purpose was served by using Raman mapping which collects huge number of spectra, and produces a complete picture of available phases along with relative variation from the reference. A detailed information about the method can be found in [46, 49–52]. The spectrum obtained at a point (cf. figure 2) was chosen as a reference, and Raman mapping was performed over the surface of the fiber as shown in figure 3.

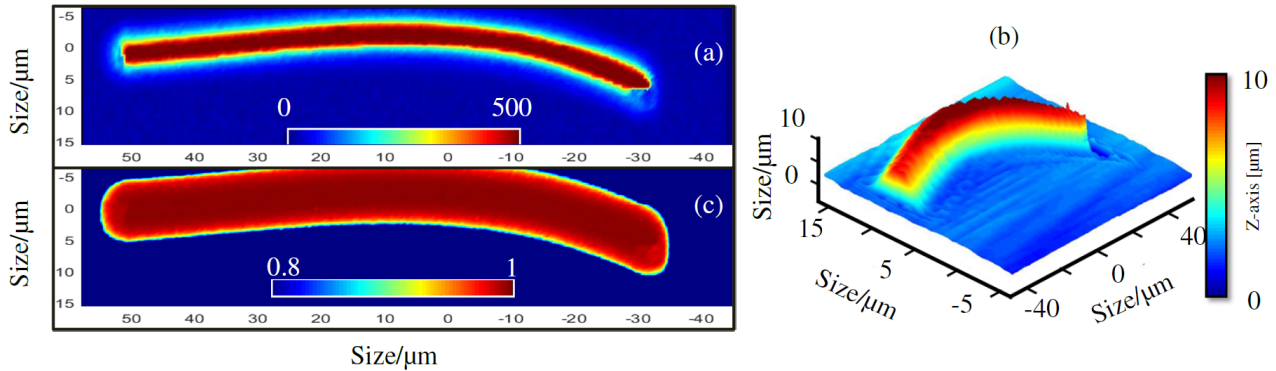


FIGURE 3 Results of Raman mapping along the axis of a r-CF obtained using Matlab software; (a) variation in G-band intensity over the surface; (b) Live track with the scale having unit in μm ; (c) DCLS analysis image.

Figure 3a displays the Raman mapping based on the intensity of G-band. On the intensity scale used, the (dark) red color represents the highest intensity of the G-band which seems to perfectly fit with the complex geometry of the analysed fiber. This was obtained by using a live tracking system which continuously adjusts the height of the motorised microscope stage to maintain the best possible focus of Raman laser during scanning. This may provide a measure of the diameter of the fiber with micrometer precision as shown in figure 3b. The latter shows the variation of the height of the microscope stage (Z-axis), which is in the range from 0-10 μm , within the analysed region. Figure 3c is reconstructed by DCLS analysis which finds a linear combination of the spectra from available components in the sample that matches with the reference spectrum as given in figure 2. The result is somehow equivalent to the plot of the intensity ratio (I_D/I_G) which is known to provide insights on the information about the structural organisation of the carbon matter. Due to spatial resolution of the spectrometer, lower absolute peak intensities of Raman spectra close to the fiber were also recorded. As a result, the size of the obtained mapping was found to be larger than the size of the fiber. Nevertheless, the structural homogeneity of a single CF can be confirmed by the uniform color of the mapping. It is worth mentioning that Raman mapping was performed over several fibers. The results of which exhibited the similar trend, hence confirming the structural homogeneity of the entire bunch of fibers.

3.2 | Description of the thermal model

The thermal conductivity was determined by first solving the steady state heat diffusion equation for a cylindrical geometry and a set of boundary conditions. Various thermal models have been used in the past for specific cases such as different geometries, boundary conditions, etc. Generally, the medium is considered as semi-infinite with three-dimensional (3-D) heat transfer in case of bulk material [29, 33], and two-dimensional (2-D) heat transfer in case of single layer graphene (SLG) [31, 34] or few layer graphene (FLG) [40]. Also, convective and radiative heat losses are generally neglected.

In case of a fiber, none of the above cases are valid as the fiber is very long as compared to its diameter which allows the majority of heat transfer along the axis of the fibers [53]. In a specific case where the flux is entering from a circular spot over the surface, heat flux line first penetrates into the sample (i.e., the thermal energy is absorbed by a small thickness), and then

travels along the longitudinal axis of the fiber (cf. figure 4). This makes it more complicated to solve the heat diffusion equation. A solution of similar problem is given by Danes et Bardon [54] where the heat diffusion equation was solved for the case of a cylinder receiving heat flux from a small area over the surface. They assimilated a fiber as a parallelepiped with sides $L1$, $L2$, and $L3$ where $L1 \approx L2 \ll L3$. The equivalent parallelepiped has the same cross-sectional area as of a fiber of diameter B (i.e., $L1.L2 = \pi B^2/4$). The uniform heat flux ϕ is imposed over a circular area of diameter D in a plane parallel to xy -plane. The right face of the parallelepiped is maintained at a prescribed temperature ($T = 0$), and the rest of the faces are considered as adiabatic i.e. no heat losses from other surfaces. Due to symmetry, only one half of the fiber is considered. The origin is defined at the center of the laser spot which is shown in red in figure 4. The equation is given as:

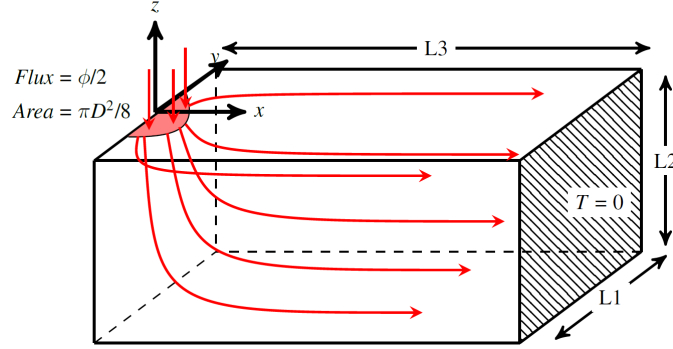


FIGURE 4 Heat transfer through a parallelepiped with heat flux entering from a circular cross-section over the surface

$$\frac{\partial^2 T}{\partial x^2} + \frac{\partial^2 T}{\partial y^2} + \frac{\partial^2 T}{\partial z^2} = 0, \quad (1)$$

with the following boundary conditions:

$$\bullet \quad -\kappa \left. \frac{\partial T}{\partial z} \right|_{z=0} = \begin{cases} \phi/2, & \text{if } 0 < r < D/2, \\ 0, & \text{if } r > D/2, \end{cases} \quad (2)$$

$$\bullet \quad x = L3, \quad T = 0, \quad (3)$$

$$\bullet \quad \text{Everywhere else, the normal temperature gradient is zero,} \quad (4)$$

where κ denotes the longitudinal thermal conductivity, r denotes the radial direction of the spot, and z denotes the depth of the material ($L2$ in this case). Also, the above equation does not take the convective and radiative heat losses into account considering that these losses are negligible. A detailed estimation of these losses will be given later in the paper. On solving the above equation, a relation between the temperature difference (ΔT) and thermal conductivity (κ) is established as follows (cf. Appendix A for detailed explanation):

$$\kappa = \frac{16P}{3\pi^2 D \Delta T} \left(1 - 0.84 \frac{D}{B} \right). \quad (5)$$

In the steady state regime, equation 5 allows to determine the thermal conductivity of a cylindrical sample by knowing the power of the heat source absorbed by the fiber (P), the temperature difference (ΔT) between two points (i.e., the source and the

sink), the diameter of the heat source (D) and the diameter of the sample (B). It is worth noting that, at a given temperature, the first term in the right hand side is related to the structural organization only, whereas the second term also considers the geometry in terms of the diameter of cylindrical sample (B). On the basis of this description, we understand why Raman spectroscopy comes to the picture because it provides the key parameters needed for the determination of thermal conductivity of fibers. Here, the Raman laser which is used to excite the samples is also used as a heat source.

3.3 | Determination of temperature difference using Optothermal Raman (OTR) technique

As known, Raman peak positions (of any material) are affected by temperature due to anharmonicity. The Raman spectroscopy which uses a laser as an excitation source was used here as a “thermometer” after a prior calibration step which involves the heating of the sample within the furnace and relates the temperature rise of the furnace with the corresponding Raman shift. Experimentally, OTR method is a two-step process as explained by Malekpour et al. [40].

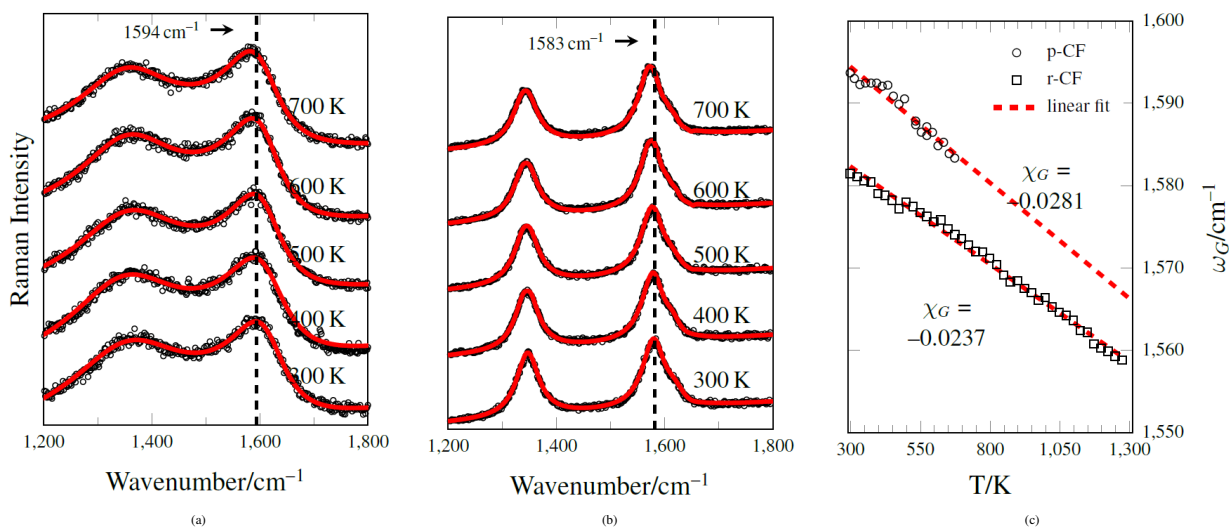


FIGURE 5 Raman spectra of CF obtained at different temperatures when the fibers were heated from the furnace; (a) PAN-based carbon fiber (p-CF) at 514.5 nm, (b) Rayon-based carbon fiber (r-CF) at 488 nm. The experimental spectra are plotted using black circles with their best fit using red lines. The shift in G-peak position (towards lower wavenumbers) can be seen from the dashed line passing through the G-peak position of Raman spectrum obtained at room temperature (300 K), (c) Linear shift of G-peak position due to heating from the furnace. The plots are for p-CF and r-CF with their corresponding linear fits. Note: for better visualization, only few spectra are shown.

- In step one**, the G-peak position was obtained as a function of sample temperature where the fibers were heated externally using a furnace (cf. figure 1). A very low laser power (≈ 0.5 mW) was used to avoid any laser induced heating. It is worth mentioning that the maximum temperature of p-CF was set to 700 K in order to avoid any structural change because of the heat treatment (as the initial heat treatment temperature is not provided by the CF manufacturer). However, the r-CF were heated up to 1300 K because these fibers were initially heat treated at 2500 K, and further heating should not make any structural change at nanometric scale. Moreover, it is notable that the band width of p-CF (cf. figure 5a) is much higher than that of r-CF (cf. figure 5b). This is related to the fact that p-CF is structurally more disordered than r-CF. This wide variation in structure is also a consequence of a high change in the G-peak positions (1594 cm^{-1} for p-CF and 1583 cm^{-1}

for r-CF which were obtained at room temperature). The analysis (cf. figure 5c) shows the values of the G-peak position (ω_G) for both CF studied as a function of furnace temperature. Due to this linear dependence, the experimental data can be fitted by using a linear function as: $\omega_G = \omega_0 + \chi_G T$, where ω_G is the G-peak positions at selected temperature (T). The slope of the linear curve ($\chi_G = \Delta\omega_G/\Delta T$), obtained from G-peak position versus temperature, allows to use Raman technique as a “thermometer”. The retrieved value of slopes of calibration curves (χ_G) of p-CF and r-CF are $-0.0281 \text{ cm}^{-1} \text{ K}^{-1}$ and $-0.0237 \text{ cm}^{-1} \text{ K}^{-1}$, respectively.

- **In step two**, the G-peak position was obtained as a function of laser power in which the surface of an isolated and suspended fiber was heated using Raman laser. For this measurement, a sample holder was designed, and the fibers were attached with silver paste suspended between two heat sinks made of copper (cf. figure 1). At the center, the fiber was locally heated using the Raman laser, whereas the heat sinks were maintained at room temperature to allow the conduction of heat along the axis of the fiber. Figure 6a and 6b show Raman spectra of p-CF and r-CF, respectively, obtained at different excitation laser powers. Similar to furnace heating, a significant shift in the G-peak position towards lower wavenumbers was observed with an increase in excitation laser power[42].

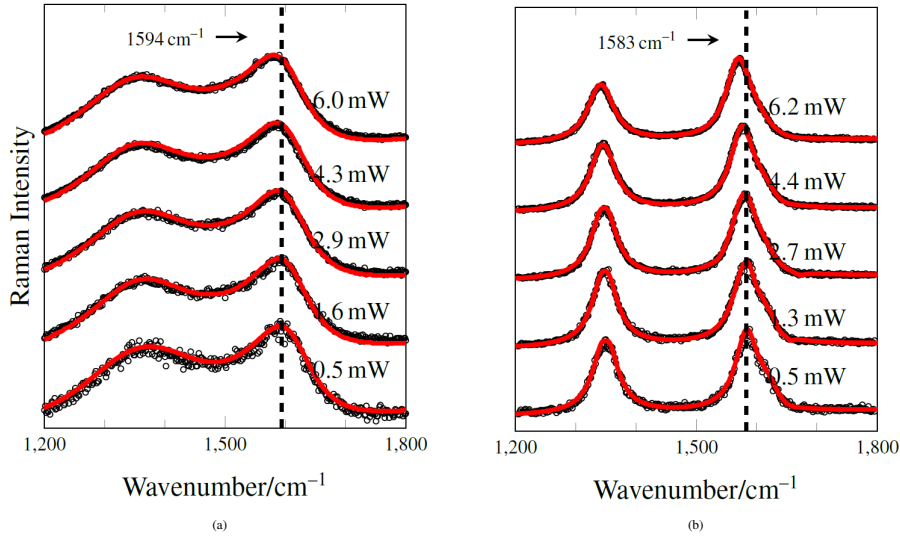


FIGURE 6 Raman spectra of CF obtained at different powers; (a) p-CF at 514.5 nm, and (b) r-CF at 488 nm. The experimental spectra are plotted using black circles with their best fit using red lines. The shift in G-peak position (towards lower wavenumbers) can be seen from the dashed line passing through the G-peak position of Raman spectrum obtained at very low laser power (0.5 mW).

The difference between the value of the G-peak position obtained at two different powers i.e., $\omega_G(P_2)$ obtained at a given power and $\omega_G(P_1)$ at a very low power (both at room temperature), is related to the temperature difference (ΔT) via the slope (χ_G) previously determined in step one as

$$\Delta T = \frac{\Delta\omega_G(P)}{\chi_G} = \frac{\omega_G(P_2) - \omega_G(P_1)}{\chi_G}. \quad (6)$$

The diameter (D) of the focused laser spot was calculated using $D = 0.61\lambda/\text{NA}$ [40, 55, 56], where NA is the numerical aperture (0.5) of the objective lens, and λ is the wavelength of the laser beam. The calculated diameter of the focused laser

spot was equal to $0.60\ \mu\text{m}$ (for $\lambda = 488\ \text{nm}$) and $0.63\ \mu\text{m}$ (for $\lambda = 514.5\ \text{nm}$). Furthermore, the laser power at the exit (P_0) was measured by a power sensor (placed after the glass window of the furnace to avoid any possible loss of laser power), and the absorbed laser power by the fibers was calculated as: $P = \alpha P_0$, where α is the local surface absorptivity (i.e., at the top part of the fiber illuminated by the incident Raman laser). This is one of the crucial parameters to determine the thermal conductivity of fibers, but due to their small size and cylindrical shape, it is extremely difficult to obtain experimentally. Therefore, the local surface absorptivity was obtained by modeling the light-matter interaction using a numerical simulation based on Monte Carlo ray tracing (MCRT) method [57–60]. The latter can be used successfully as the fiber satisfies the geometric optics approximation (GOA) i.e., the size parameter ($\pi B/\lambda \gg 1$) [57]. Figure 7 depicts the 2D view of ray tracing procedure in which the top surface of the fiber is illuminated as in case of Raman spectroscopy. Similar to experimental conditions, a conical beam with Gaussian distribution over the laser spot has been considered, and 10^6 number of rays were used for better accuracy [60]. Also, the surface of the fiber is considered as optically smooth.

As used in this work, the ray tracing simulation requires the knowledge of optical properties i.e., $n \pm ik$ where ‘ n ’ and ‘ k ’ are the index of refraction and absorption, respectively, to calculate the local specular reflectivity at a given incidence angle (θ_i). More details on the numerical method can be found in references [58, 61]. Based on the type of the fibers used and the structural analysis performed by Raman spectroscopy, the optical properties of glassy carbon were selected [62]. Finally, the local surface absorptivity was calculated by summing all the individual directional absorptivities which comes out to be 0.863. This was deduced by making the energy balance, and the directional transmissivity was considered as zero due to high value of ‘ k ’. This value is in good agreement with the literature [14]. It is worth mentioning that, due to small angles of incidence (θ_i), the calculated local surface absorptivity is equal to the normal surface absorptivity [57] (corresponding to a flat and optically smooth surface). This confirms that the effect of curvature is negligible in our case. Furthermore, owing to the fact that the optical properties of sp^2 carbons do not vary significantly with temperature at given wavelengths [63], the local surface absorptivity can be considered as constant within the temperature range from 300-1300 K [64, 65].

Once all the required data was collected, equation (6) and (5) were used to determine the thermal conductivity of CF as a function of temperature.

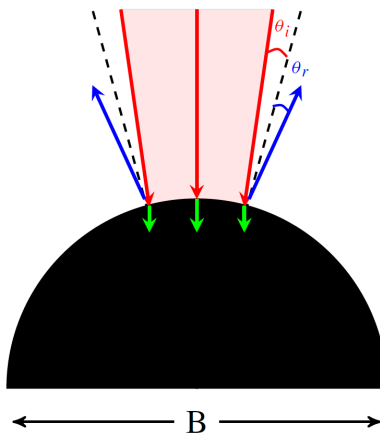


FIGURE 7 2D schematic of the Monte Carlo ray tracing process. The incident (red) and reflected (blue) rays are shown for the reference. Green arrows represent the energy absorbed by the fiber. θ_i and θ_r are the incident and reflection angles from the surface normal shown in dashed lines, respectively.

Figure 8 shows the evolution of thermal conductivity with temperature. For statistical representation, four fibers were tested. The mean value and standard deviation of their thermal conductivity are plotted. The thermal conductivity of p-CF (cf. figure

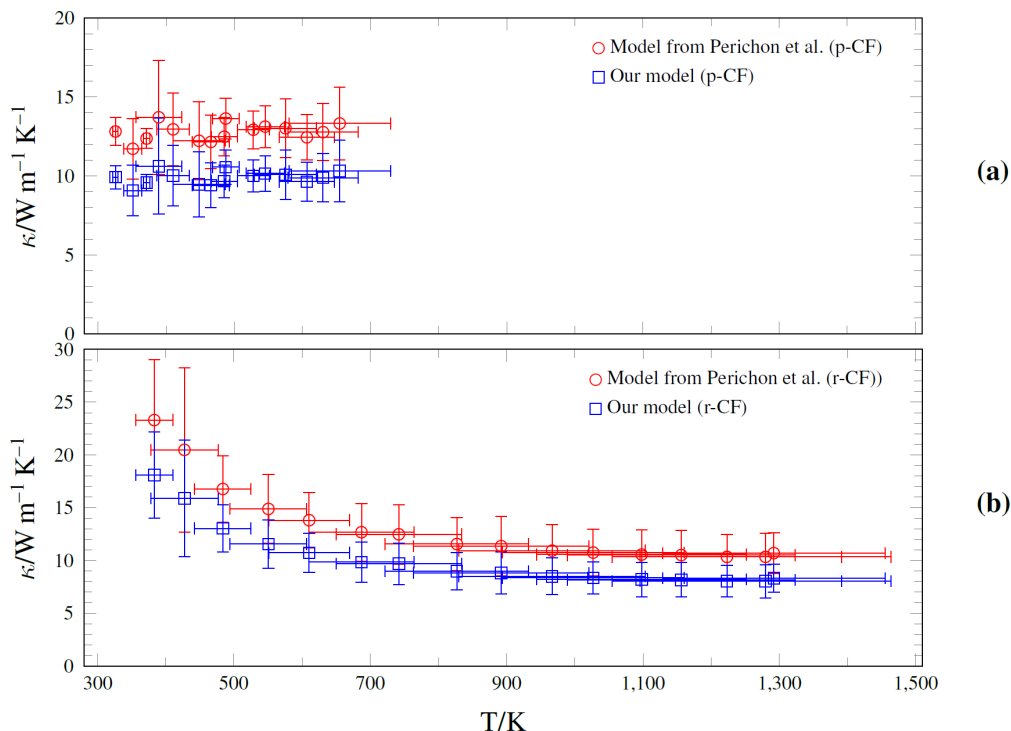


FIGURE 8 Temperature dependence of thermal conductivity of p-CF (top) and r-CF (bottom) calculated using the thermal model given by Perichon et al. [29] (in red), and our thermal model (in blue).

8a) in the measured range of temperature from 300-700 K shows a slight increase with temperature. However, the thermal conductivity of r-CF (cf. figure 8b) decreases rapidly up to ≈ 800 K, and then becomes almost constant.

The variation of the thermal conductivity of the two CF used in this study can be explained by Umklapp and defect scatterings. Generally, at low temperatures, as the specific heat increases with the increase in temperature, the thermal conductivity is expected to increase continually [66]. However, this increase in temperature induces the scattering of phonons by phonons (known as Umklapp scattering) which decreases the phonon mean free path and has the consequence of lowering the thermal conductivity at high temperatures. For example, in highly ordered sp^2 carbons, starting from absolute zero, the thermal conductivity first increases rapidly with the increase in temperature until it reaches a maximum value, and beyond that temperature, thermal conductivity decreases exponentially [67]. Moreover, the thermal conductivity and its maximum value, as mentioned previously, appear to be strongly affected by defects (either point or boundary) and disorder present in solid carbon since phonons may also be scattered by them. The contribution of these defects to the thermal conductivity of the material can be added in reciprocal manner. Rigorous work has been done in the past on the estimation of the contribution of these defects to thermal conductivity [67, 68]. Kelly et al. showed from calculation that the crystallite boundaries have the most significant contribution in phonon scattering [68]. Based on above explanation from the literature, it could be concluded that, as the crystallite size increases, the thermal conductivity increases and the thermal conductivity peak shifts to a lower temperature [68–70]. In addition, Yamane et al. [15] performed a series of experiments to understand the effect of temperature on the thermal conductivity of different polyacrylonitrile (PAN) based CF (supplied from Toray Industries, Inc.) having different degrees of structural organization. Their results state that the thermal conductivity of fibers with low crystallite size such as T300 (or p-CF as used in this work) and T800H, increases with temperature throughout the measured range of temperature from 300-800 K, and showing a weakly linear trend. However, for fibers having high crystallite sizes, the thermal conductivity first significantly increases with temperature, and then decreases. Also, they observed a significant shift in the peak position towards a higher temperature as the crystallite size

increases [68]. Coming back to our results, above explanation shows why the thermal conductivity of r-CF, which were initially heat treated at 2500 K, decreases with the increase in temperature within the measured range of temperature from 300-1300 K. In comparison to that, the thermal conductivity of p-CF shows weakly linear trend.

One of the main challenges while using OTR method is the validity of the thermal model used for the determination of thermal conductivity. For comparison, two different thermal models were used: the thermal model given by Périchon et al. [29] which considers the medium as semi-infinite with 3-D heat transfer while our model (cf. equation (5)) considers the medium as long infinite cylinder with 3-D heat transfer in the vicinity of the laser spot (which then follows the axis). The results confirm that the thermal conductivity estimated using the model described by Périchon et al. provides the results $\approx 30\%$ higher than our model (equation (5)). This can be explained by the fact that our model considers the geometry of the fiber in terms of its diameter (B) which is not considered in case of the model described by Périchon et al., and supposed to describe more appropriately the heat transfer through a fiber heated locally.

Additionally, the results obtained for thermal conductivity of p-CF using our model were cross-validated with the data published in the literature [22, 43] for the same type of fibers i.e., T300. The method used by Mishra et al. [22], for the measurement of thermal conductivity, is specified as 3ω . However, the method used by the manufacturer [43] is not specified. The results obtained in this work for the thermal conductivity of p-CF at room temperature is shown in table 1. Our results obtained using OTR technique show a good agreement with references [22, 43] with less than 5% discrepancy.

Method used	OTR	3ω	Not specified
Reference	This work	[22]	[43]
κ (W m ⁻¹ K ⁻¹)	10	10.2	10.5

TABLE 1 Thermal conductivity of p-CF at room temperature in comparison with the literature values.

4 | ESTIMATION OF HEAT LOSSES

Despite the use of highly accurate instruments and experimental setup, there is a scope for uncertainty. This can be due to the measurement errors such as imperfection of laser focus, and heat losses due to thermal radiation and/or convection. However, the heat losses are generally neglected, which may result in an over-estimated value of thermal conductivity depending on the amount of heat loss. Hence, these losses should not be neglected. These uncertainties have been discussed in several literature such as [19, 71–74] and in this work, we estimated the amount of these losses and their effects.

Li et al. [73, 74] estimated the radiative heat losses by using the Stefan-Boltzmann law which is:

$$Q_{\text{rad}} = \sigma \epsilon S (T_{\text{avg}}^4 - T_0^4) \simeq h_r (T_{\text{avg}} - T_0), \quad (7)$$

where $\sigma = 5.67 \times 10^{-8} \text{ W m}^{-2} \text{ K}^{-4}$, is the Stefan-Boltzmann constant, ϵ is the apparent emissivity of the fiber, S is the total lateral surface area (πBL , where L is the length) of the fiber, T_{avg} is the average temperature of the fiber, T_0 is the surrounding temperature, $h_r = 4\sigma \epsilon T_m^3$, is the radiative heat transfer coefficient, and $T_m = (T_{\text{avg}} + T_0)/2$, is the mean temperature. Here, the term ‘apparent’ is used because it includes the radiation going out in all the directions (i.e., entire 4π steradian). ϵ is computed using previously mentioned MCRT method with a beam diameter equivalent to that of Raman laser. Its value comes out to be 0.859 at 300 K. As for the local surface absorptivity, we assume that at $T = 1300$ K, the apparent emissivity remain same.

Furthermore, to calculate T_{avg} , knowing that the temperature is known at the laser spot (T_{max}) and at ends (T_0) of the fiber, the heat diffusion equation was solved for the case of cylindrical rod with convective and radiative heat losses from the surface and the mean temperature (T_{avg}) can be calculated as

$$T_{\text{avg}} = T_0 + \frac{(T_{\text{max}} - T_0)}{mL} \left[\sinh(mL) - \coth(mL)(\cosh(mL) - 1) \right] \quad (8)$$

where $m = \sqrt{hp/\kappa A_c}$, p is the parameter (πB), A_c is the cross-sectional area ($\pi B^2/4$), $h = h_c + h_r$ with h_c and h_r are convective and radiative heat transfer coefficients, respectively. One could refer to Incropera et al. [75] for detailed explanation about the formulation.

Furthermore, the heat losses from natural convection are negligible at microscale because buoyancy, the driving force for natural convection, is very small as concluded by Guo et al. [76] and Wang et al. [72]. The loss can be calculated by taking the ratio of radiative heat loss to heat generation (Q_{rad}/Q). The heat generation is considered equivalent to the power of the laser absorbed by the fibers ($Q = P$). The maximum loss due to radiation, at a temperature of 1300 K, for a computed value of emissivity ($\epsilon = 0.859$), 1 mm in length and 6 μm in diameter having a surface area of $1.9 \times 10^{-8} \text{ m}^2$, comes out to be less than 2.95 % of the total power absorbed.

Errors due to heat losses depend on factors: the diameter and the length of the fibers used for measurement. These losses can be reduced by reducing these factors. This aspect was considered before performing the experiment, and the length used for the measurement was ≈ 1 mm as compared to several cm's used in other works, thereby reducing the overall error.

5 | CONCLUSION

In this paper, an optical method based on Raman spectroscopy is presented to measure the longitudinal thermal conductivity of micrometric sized CF in a temperature range varying from 300-1300 K. In particular, Raman mapping was first used to analyze the structure and its homogeneity, which was then extended to determine the thermal conductivity using OTR technique. Raman spectroscopy confirmed that the fibers are not very well structured and contain a significant amount of defects. The defect density is higher for p-CF as compared to for r-CF. Furthermore, Raman mapping confirmed the structural homogeneity of the fibers. Therefore, the thermal conductivity measured using OTR will be the representative of the whole fiber.

The heat diffusion equation was solved for a specific case of the fiber and a set of boundary conditions similar to the one in the experiment. The results were calculated using two models: one for bulk material and other for fibers. It was found that the bulk material relation provides results ≈ 30 % higher than our model because it considers that the heat is uniformly distributed in all three directions instead of (majority in) one direction as in case of fibers.

The method is able to determine the thermal conductivity of CF as a function of temperature over a wide range of temperature. In particular, it was found that the thermal conductivity of r-CF is higher than that of p-CF at room temperatures. The initially heat treated r-CF possess low defect density (i.e., larger crystallite size) as compared to p-CF, therefore the mean free path of phonons is longer, giving a higher value of thermal conductivity.

The behavior of thermal conductivity as a function of temperature was observed for two different fibers. It was found that the thermal conductivity of p-CF increases slightly in the temperature range from 300-700 K, while it decreases for r-CF in the temperature of 300-1300 K. This behavior is in good agreement with the literature. Also, to ensure the accuracy of the experiment, the thermal conductivity of p-CF obtained at room temperature was compared with literature data. The results are in good agreement, hence validating our approach. The role of convective and radiative heat losses was also determined. The total losses are less than 3 % because of the small length and diameter of fibers used for measurement.

It is evident that Raman spectroscopy is not only reliable for structural characterization, but it can also be used for determination of thermophysical properties such as the thermal conductivity of microscopic samples over a wide range of temperatures by producing results with high accuracy which is rather difficult to obtain with other methods. In addition to that, our thermal model can be used for any cylindrical geometry. This study was limited to the measurement of low ordered CF due to their specific applications but further measurements on highly ordered CF would be interesting and provide the scope of future work.

Some limitations were faced at high temperatures. As the sample reached near 1300 K, the thermal emission becomes high and the required Raman signals are eventually lost. In such cases, lower excitation laser wavelengths such as UV laser can be of utmost importance to attain higher temperatures, since Raman spectrum will be recorded in the wavelength range away from the point at which the thermal radiation is maximum. Moreover, the efficiency of scattering is increased by the forth power of wavelength thus the use of shorter excitation wavelengths significantly increase Raman intensity. These minimal changes will extend the boundaries of the current work and also provide scope for future enhancements.

ACKNOWLEDGEMENTS

A. Kumar would like to thank Mersen, Gennevilliers, France and National Association for Research and Technology (ANRT) for funding his research during the Ph.D. under the Industrial Agreement of Training through Research (CIFRE). The author also thanks Dr. Patrick Simon, CEMHTI, Orléans, France and Dr. Denis Rochais, CEA, Monts (37), Dr. Gerard L. Vignoles and Georges Chollon, LCTS, Bordeaux, France for fruitful and valuable discussions and Jérôme Delmas, technician, LTeN, Nantes, France for his help to prepare sample holders used for the measurements. The financial support of the French Agency for Research (Agence Nationale de la Recherche, ANR) is also acknowledged through the Equipex Planex ANR-11-EQPX-36.

AUTHOR CONTRIBUTIONS STATEMENT

A.K. carried out the experiment, analyzed the data, worked on thermal model, and wrote the manuscript. M.R.A. supervised the research, developed the experiment, verified the data, and edited the manuscript. A.C. helped to setup the experiment. J.V. partially supervised the research. B.R. proposed the idea, edited the manuscript, and directed the research. All authors discussed the results and reviewed the manuscript.

COMPETING INTERESTS

The authors declare no competing interests.

APPENDIX A : HEAT TRANSFER THROUGH A CYLINDER WITH HEAT SUPPLY FROM A CIRCULAR AREA OVER THE SURFACE

The solution of heat diffusion equation (cf. equation 1 in the main manuscript) for a semi-infinite medium with constant heat flux entering from the circular area over the surface was originally given by Carslaw and Jaeger [77]. They used the Hankel transformation to transform the partial differential equation into ordinary differential equation, and determined the average temperature (T_{avg}) over $0 < r < D/2$ or the temperature difference (ΔT) as:

$$T_{\text{avg}} = \Delta T = \frac{8\phi R}{3\pi\kappa}. \quad (9)$$

where ϕ is the flux uniformly distributed over the circular area of radius R (or laser spot). However, in case of laser with Gaussian distribution, the difference is significantly small (i.e., $\approx 0.53\%$ as given by Huang et al. [33]). Furthermore, the constriction resistance can be written as:

$$R_c = \frac{\Delta T}{(\pi R^2)\phi/2} = \frac{16}{3\pi^2 R\kappa}. \quad (10)$$

The above formulations are valid only if the heat flux entering from a circular area is dissipated uniformly in all the directions. In case of a parallelepiped (cf. figure 3 in the main manuscript), where $L1 \approx L2 \ll L3$, heat flux lines first penetrate up to a certain depth and then travel through the axis of the fiber. The total constriction resistance which is determined by *source and sink method* will be the sum of following contributions:

- due to heat transfer through the semi-infinite medium (cf. equation (10)),
- due to constriction causing the heat flux lines to follow the longitudinal axis of parallelepiped as given by Danes et al. [54].

Summing up the above mentioned resistances and for a specific case when the length of fiber between two contact points ($2 \times L3$) \gg diameter of fiber (B), one gets the following equation:

$$R_c = \frac{F_{CO}}{\kappa} = \frac{16}{3\pi^2 R\kappa} [1 - \alpha K(\beta)], \quad (11)$$

where F_{CO} is the constriction function, R is the contact radius, and α is the ratio of the contact radius to the fiber radius. The finite width correction factor $K(\beta)$ is given as:

$$K(\beta) = \frac{3\pi^2}{16} \left(\frac{\beta}{0.19215(\beta + 2)^2 + 0.47924\beta} \right), \quad (12)$$

where β is the length ratio ($L1/L2$) which is 1 for the fiber of circular cross-section which gives $K(\beta) = 0.837887$. Using equation (11) and (12), the temperature difference ΔT because of the heat flux entered from the semicircular area is:

$$\Delta T = R_c \times \frac{\phi}{2} (\pi R^2), \quad (13)$$

$$\Delta T = \frac{8\phi R}{3\pi\kappa} \left(1 - 0.83788 \frac{D}{B} \right). \quad (14)$$

Or, writing the above equation in terms of the diameter $D = 2R$,

$$\kappa = \frac{4\phi D}{3\pi\Delta T} \left(1 - 0.83788 \frac{D}{B} \right). \quad (15)$$

In other words, the rate of heat flow (power) over the circle of radius R is $P = \frac{\pi D^2 \phi}{4}$ which gives:

$$\kappa = \frac{16P}{3\pi^2 D \Delta T} \left(1 - 0.83788 \frac{D}{B}\right), \quad (16)$$

where D is the diameter of the source and B is the diameter of the fiber.

REFERENCES

- Hailin Cong, Jianmin Zhang, Maciej Radosz, Youqing Shen, *Journal of Membrane Science* **2007**, 294 (1-2), 178–185.
- Peihong Chen, Mark A. Fryling, Richard L. McCreery, *Analytical Chemistry* **1995**.
- Qian Deng, Xinyang Li, Jiane. Zuo, Alison Ling, Bruce E. Logan, *Journal of Power Sources* **2010**, 195 (4), 1130–1135.
- John D Buckley, Dan D Edie, *Carbon-carbon materials and composites, Vol. 1254*, William Andrew, **1993**.
- Xiang Xiong, Bai-yun Huang, Jiang-hong Li, Hui-juan Xu, *Carbon* **2006**, 44 (3), 463–467.
- Bernd Helber, Olivier Chazot, Annick Hubin, Thierry E. Magin, *Composites Part A: Applied Science and Manufacturing* **2015**, 72, 96–107.
- Arnaud Borner, Francesco Panerai, Nagi N. Mansour, *International Journal of Heat and Mass Transfer* **2017**, 106, 1318–1326.
- Nikhil Banerji, Pénélope Leyland, Sophia Haussener, *Carbon* **2017**, 451–461.
- L. Paglia, J. Tirillò, F. Marra, C. Bartuli, A. Simone, T. Valente, G. Pulci, *Materials & Design* **2016**, 90, 1170–1180.
- Atin Kumar, Jérôme Vicente, Jean-Vincent Daurelle, Yann Favennec, Benoit Rousseau, *Heat and Mass Transfer* **2023**, 1–23.
- R I Baxter, R D Rawlings, N Iwashita, Y Sawada, *Carbon* **2000**, 38 (3), 441–449.
- Francesco Panerai, Joseph C. Ferguson, Jean Lachaud, Alexandre Martin, Matthew J. Gasch, Nagi N. Mansour, *International Journal of Heat and Mass Transfer* **2017**, 108, 801–811.
- Yann Dauvois, Denis Rochais, Franck Enguehard, Jean Taine, *International Journal of Heat and Mass Transfer* **2017**, 106, 601–618.
- Yo-Rhin Rhim, Dajie Zhang, Michael Rooney, Dennis C Nagle, D Howard Fairbrother, Cila Herman, David G. Drewry, *Carbon* **2010**, 48 (1), 31–40.
- Tsuneyuki Yamane, Shin Ichiro Katayama, Minoru Todoki, Ichiro Hatta, *Journal of Applied Physics* **1996**.
- T Yamane, S Katayama, M Todoki, I Hatta, *Journal of Wide Bandgap Materials* **2000**, 7 (4), 294–305.
- C. Pradere, J. C. Batsale, J. M. Goyhèneche, R. Paillet, S. Dilhaire, *Carbon* **2009**, 47 (3), 737–743.
- D. Rochais, H. Le Houédec, F. Enguehard, J. Jumel, F. Lepoutre, *Journal of Physics D: Applied Physics* **2005**, 38 (10), 1498–1503.
- L. Lu, W. Yi, D. L. Zhang, *Review of Scientific Instruments* **2001**, 72 (7), 2996–3003.
- Lin Qiu, Hanying Zou, Ning Zhu, Yanhui Feng, Xiaoliang Zhang, Xinxin Zhang, *Applied Thermal Engineering* **2018**, 141, 913–920.
- Lin Qiu, Hanying Zou, Xiaotian Wang, Yanhui Feng, Xinxin Zhang, Jingna Zhao, Xiaohua Zhang, Qingwen Li, *Carbon* **2019**, 141, 497–505.
- Ketaki Mishra, Bertrand Garnier, Steven Le Corre, Nicolas Boyard, *Journal of Thermal Analysis and Calorimetry* **2020**, 139 (2), 1037–1047.
- Olaya Rodrigo, Bertrand Garnier, *International Journal of Thermal Sciences* **2023**, 193, 108510.
- Jianli Wang, Bai Song, Xing Zhang, Yang Song, Gangping Wu, *International Journal of Thermophysics* **2011**, 32 (5), 974.
- Jinhui Liu, Haidong Wang, Yudong Hu, Weigang Ma, Xing Zhang, *Review of Scientific Instruments* **2015**, 86 (1), 014901.
- N.C. Gallego, D.D. Edie, B. Nysten, J.P. Issi, J.W. Treleaven, G.V. Deshpande, *Carbon* **2000**, 38 (7), 1003–1010.
- Dongliang Zhao, Xin Qian, Xiaokun Gu, Saad Ayub Jajja, Ronggui Yang, *Journal of Electronic Packaging* **2016**.
- Yifeng Fu, Josef Hansson, Ya Liu, Shujing Chen, Abdelhafid Zehri, Majid Kabiri Samani, Nan Wang, Yuxiang Ni, Yan Zhang, Zhi-Bin Zhang, et al., *2D Materials* **2019**, 7 (1), 012001.
- S. Périchon, V. Lysenko, B. Remaki, D. Barbier, B. Champagnon, *Journal of Applied Physics* **1999**, 86 (8), 4700–4702.
- V Lysenko, S Perichon, B Remaki, D Barbier, B Champagnon, *Journal of Applied Physics* **1999**, 86 (12), 6841–6846.
- Alexander A Balandin, Suchismita Ghosh, Wenzhong Bao, Irene Calizo, Desalegne Teweldebrhan, Feng Miao, Chun Ning Lau, *Nano Lett.* **2008**.
- D. L. Nika, E. P. Pokatilov, A. S. Askerov, A. A. Balandin, *Physical Review B - Condensed Matter and Materials Physics* **2009**.
- Shuo Huang, Xiao-dong Ruan, Xin Fu, Hua-yong Yang, *Journal of Zhejiang University Science A* **2009**, 10 (1), 7–16.
- Jae Ung Lee, Duhee Yoon, Hakseong Kim, Sang Wook Lee, Hyeonsik Cheong, *Physical Review B - Condensed Matter and Materials Physics* **2011**, 83 (8).
- Alexander A Balandin, *Nature materials* **2011**, 10 (8), 569.
- S. Ghosh, I. Calizo, D. Teweldebrhan, E. P. Pokatilov, D. L. Nika, A. A. Balandin, W. Bao, F. Miao, C. N. Lau, *Applied Physics Letters* **2008**.
- Jackie D Renteria, Sylvester Ramirez, Hoda Malekpour, Beatriz Alonso, Alba Centeno, Amaia Zurutuza, Alexandr I Cocemasov, Denis L Nika, Alexander A Balandin, *Advanced Functional Materials* **2015**, 25 (29), 4664–4672.
- Hoda Malekpour, Pankaj Ramnani, Srilok Srinivasan, Ganesh Balasubramanian, Denis L Nika, Ashok Mulchandani, Roger K Lake, Alexander A Balandin, *Nanoscale* **2016**, 8 (30), 14608–14616.
- S. Venkatachalam, M. Depriester, A. Hadj Sahrhoui, B. Capoen, M. R. Ammar, D. Hourlier, *Carbon* **2017**, 114, 134–140.
- Hoda Malekpour, Alexander A Balandin, *Journal of Raman Spectroscopy* **2018**, 49 (1), 106–120.
- Fariborz Kargar, Ece A Coleman, Subhajit Ghosh, Jonathan Lee, Michael J Gomez, Yuhang Liu, Andres Sanchez Magana, Zahra Barani, Amirmahdi Mohammadzadeh, Bishwajit Debnath, et al., *ACS nano* **2020**, 14 (2), 2424–2435.
- N.J. Everall, J. Lumsdon, D.J. Christopher, *Carbon* **1991**, 29 (2), 133–137.
- Toray Carbon Fibers America, *Toray Inc., T300 data sheet, Technical data sheet, No.: CFA-001*, https://www.toraycma.com/file_viewer.php?id=4462.
- D De Sousa Meneses, *Software Utility for the Creation of Optical Function (FOCUS), CEMHTI UPR 3079 CNRS Orléans, France*, <https://www.cemhti.cnrs-orleans.fr/pot/software/focus.html>, **2004**.
- F. Tuinstra, J. L. Koenig, *The Journal of Chemical Physics* **1970**, 53 (3), 1126–1130.
- Djamila Hourlier, Srisaran Venkatachalam, Mohamed Ramzi Ammar, Yigal Blum, *Journal of Analytical and Applied Pyrolysis* **2017**.
- Y Hbiriq, MR Ammar, C Fantini, L Hennet, M Zaghioui, *Physical Review B* **2023**, 107 (13), 134305.
- M. R. Ammar, N. Galy, J. N. Rouzaud, N. Toulhoat, C. E. Vaudey, P. Simon, N. Moncoffre, *Carbon* **2015**, 95, 364–373.
- Rudy Michel, Mohamed Ramzi Ammar, Jacques Poirier, Patrick Simon, *Ceramics International* **2013**, 39 (5), 5287–5294.
- Frédéric Foucher, Guillaume Guimbretière, Nicolas Bost, Frances Westall, *Raman spectroscopy and applications. IntechOpen, London* **2017**, 163–180.

51. Chunxiao Cong, Kun Li, Xi Xiang Zhang, Ting Yu, *Scientific reports* **2013**, 3, 1195.
52. Olga A Maslova, G Guimbretière, MR Ammar, L Desgranges, C Jégou, A Canizarès, P Simon, *Materials Characterization* **2017**, 129, 260–269.
53. Dawon Jang, Dong Su Lee, Aram Lee, Han-Ik Joh, Sungho Lee, *Journal of Industrial and Engineering Chemistry* **2019**, 78, 137–142.
54. Florin Danes, Jean-Pierre Bardon, *Revue générale de thermique* **1997**, 36 (4), 302–311.
55. Rusen Yan, Jeffrey R Simpson, Simone Bertolazzi, Jacopo Brivio, Michael Watson, Xufei Wu, Andras Kis, Tengfei Luo, Angela R Hight Walker, Huili Grace Xing, *ACS nano* **2014**, 8 (1), 986–993.
56. Weiwei Cai, Arden L Moore, Yanwu Zhu, Xuesong Li, Shanshan Chen, Li Shi, Rodney S Ruoff, *Nano letters* **2010**, 10 (5), 1645–1651.
57. Michael F Modest, *Radiative heat transfer*, Academic press, **2013**.
58. Benoit Rousseau, Domingos de Sousa Meneses, Patrick Echegut, Marco Di Michiel, Jean-François Thovert, *Applied optics* **2007**, 46 (20), 4266–4276.
59. B Rousseau, H Gomart, D Zanghi, D Bernard, M Stampanoni, *Journal of materials research* **2010**, 25 (10), 1890–1897.
60. Simon Guévelou, Benoit Rousseau, Gilberto Domingues, Jérôme Vicente, Cyril Caliot, *International Journal of Heat and Mass Transfer* **2016**, 93, 118–129.
61. Benoit Rousseau, Marco Di Michiel, Aurélien Canizares, Domingos De Sousa Meneses, Patrick Echegut, Jean François Thovert, *Journal of Quantitative Spectroscopy and Radiative Transfer* **2007**, 104 (2), 257–265.
62. MW Williams, ET Arakawa, *Journal of Applied Physics* **1972**, 43 (8), 3460–3463.
63. B. J. Stagg, T. T. Charalampopoulos, *Combustion and Flame* **1993**, 94 (4), 381–396.
64. Violaine Le Louët, Benoit Rousseau, Steven Le Corre, Nicolas Boyard, Xavier Tardif, Jérôme Delmas, Didier Delaunay, *International Journal of Heat and Mass Transfer* **2017**, 112, 882–890.
65. E Brodu, M Balat-Pichelin, D De Sousa Meneses, J-L Sans, *Carbon* **2015**, 82, 39–50.
66. M. G. Holland, *Physical Review* **1963**, 132 (6), 2461–2471.
67. R. Taylor, S. B. Venkata Siva, P. S. Rama Sreekanth, *Carbon matrix composites*, Elsevier Ltd., **2018**.
68. B.T Kelly, K.E Gilchrist, *Carbon* **1969**, 7 (3), 355–358.
69. JC Bokros, LD LaGrange, FJ Schoen, *New York: Dekker* **1969**, 5, 1–118.
70. Roy Taylor, Stephen P Turner, Kevin Garner, Xiang X Jiang, *High Temperatures. High Pressures* **1993**, 25 (4), 443–450.
71. Jinhui Liu, Hao Liu, Weigang Ma, Xing Zhang, *Review of Scientific Instruments* **2019**, 90 (4), 044901.
72. Z.L. Wang, D.W. Tang, *International Journal of Thermal Sciences* **2013**, 64, 145–151.
73. Qin-Yi Li, Xing Zhang, *Thermochimica Acta* **2014**, 581, 26–31.
74. Changzheng Li, Shen Xu, Yanan Yue, Bing Yang, Xinwei Wang, *Carbon* **2016**, 103, 101–108.
75. Frank P Incropera, Adrienne S Lavine, Theodore L Bergman, David P DeWitt, *Fundamentals of heat and mass transfer*, Wiley, **2007**.
76. Zeng-Yuan Guo, Zhi-Xin Li, *International journal of heat and mass transfer* **2003**, 46 (1), 149–159.
77. J. C. Jaeger H. S. Carslaw, *Oxford: Clarendon Press, 2nd. edit.* **1959**, 255.

Acronyms

BWF Breit-Wigner-Fano 3

CCD charged coupled device 2

CF carbon fiber 1, 2, 4, 5, 7–10, 12, 13

DCLS direct classical least square 3, 5

FLG few layer graphene 5

FWHM full width at half maximum 3

GOA geometric optics approximation 9

MCRT Monte Carlo ray tracing 9, 11

OTR Optothermal Raman 2, 3, 7, 11, 12

PAN polyacrylonitrile 10

p-CF PAN-based carbon fiber 2, 7–12

r-CF rayon-based carbon fiber 2, 4, 5, 7, 8, 10–12

SLG single layer graphene 2